

LOCAL ENTRAINMENT AND DETRAINMENT IN TURBULENT PLANAR JETS

Tai Wada

Department of Aeronautics
 Imperial College London
 SW7 2AZ London, United Kingdom
 t.wada@imperial.ac.uk

J.C. Vassilicos

Department of Aeronautics
 Imperial College London
 SW7 2AZ London, United Kingdom
 j.c.vassilicos@imperial.ac.uk

ABSTRACT

We develop a theoretical method to derive the scalings of the turbulent/non-turbulent interface (TNTI) local entrainment velocity for self-similar turbulent planar jets and also use elements of this method to develop a robust way of estimating this local TNTI velocity from Direct Numerical Simulations (DNS) of a turbulent planar jet. Our DNS supports our theoretical assumptions and predictions, in particular the link between TNTI entrainment and the equilibrium/non-equilibrium nature of the turbulence dissipation. Tracking of fluid elements which cross the TNTI reveal the existence of a small number of detrainment events and of a small number of fluid elements which undergo a series of entrainment/detrainment TNTI crossings.

Jet growth and Dissipation Scaling

In this work we study turbulent planar jets theoretically and computationally. The jet width δ and the centerline velocity u_C of self-similar planar jets obey the following scalings with streamwise distance x from the jet nozzle exit; $\delta(x)/H \sim (x-x_0)/H$ and $u_C(x)/U_J \sim ((x-x_0)/H)^{-1/2}$ (where H is the jet opening width, U_J is the inlet characteristic velocity and x_0 is a virtual origin), provided that the centerline turbulent dissipation rate scales as $\epsilon_0 = C_\epsilon K_0^{3/2}/\delta$ where C_ϵ is the dissipation constant and K_0 is the centerline turbulent kinetic energy (Townsend (1976), George (1989)). However a different dissipation scaling has recently been found in various turbulent flows including planar jets (Dairay *et al.* (2015), Vassilicos (2015), Cafiero & Vassilicos (2019)). This non-equilibrium turbulence dissipation scaling is

$$\epsilon_0 \sim (Re_G/Re_\delta)^m K_0^{3/2}/\delta \quad (1)$$

where $Re_G = U_J H/\nu$ is the global Reynolds number, $Re_\delta = \sqrt{K_0}\delta/\nu$ is the local Reynolds number and m is the non-equilibrium dissipation scaling exponent. This implies revised jet growth and centerline velocity decay rates

$$\delta(x)/H \sim ((x-x_0)/H)^{2a} \quad (2)$$

$$u_C(x)/U_J \sim ((x-x_0)/H)^{-a} \quad (3)$$

where $2a = (m+1)/(2m+1)$. The classical scalings are recovered for $m=0$, and the high Reynolds number non-equilibrium scaling corresponds to $m=1$. For $m=1$, the scalings of the jet growth and the centerline velocity decay rates are $\delta(x)/H \sim ((x-x_0)/H)^{0.66}$ and $u_C(x)/U_J \sim ((x-x_0)/H)^{-0.33}$.

DNS of a planar jet

We have carried out a Direct Numerical Simulation (DNS) of a planar jet using the sixth order finite difference Navier Stokes solver "Incompact3d". We conducted two different simulations, DNS3000 and DNS4000, with different Reynolds numbers and boundary (entrainment) conditions. The domain sizes and grid resolutions are $L_x, L_y, L_z = (40H, 40H, 8H), (40H, 80H, 8H)$ and $N_x, N_y, N_z = (1501, 1501, 300), (1501, 2001, 300)$ for DNS 3000 and DNS4000 respectively. The computational grid is homogeneous in the x (streamwise) and z (spanwise) directions. Lateral (y) direction grid is also homogeneous for DNS3000 but it is stretched for DNS4000. We used a channel flow profile with artificial turbulence (see Klein *et al.* (2003)) as jet inlet and the convective boundary condition at the outlet. The inlet Reynolds number is $Re_G = 3000$ for DNS3000 and $Re_G = 4000$ for DNS4000. We imposed free-slip boundary condition at the lateral boundary for DNS4000 and Neumann condition for DNS3000. Periodic boundary conditions are imposed at the spanwise direction boundaries. Our two DNS return different decays of the mean velocity and different jet width growths. They are compared with reference experiments and DNS (Thomas &

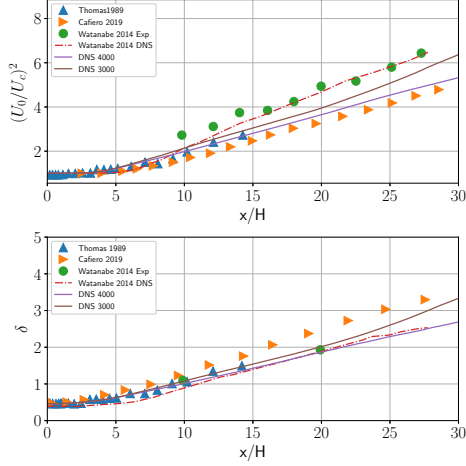


Figure 1. Jet velocity decay and width growth for DNS3000 and DNS4000 and various other simulations and experiments.

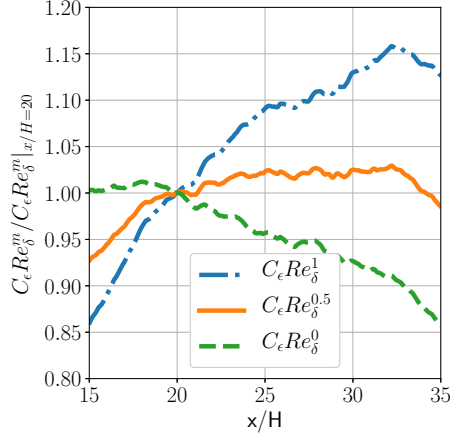


Figure 2. $C_\epsilon Re_\delta^m$ plotted along x/H (normalized by the value at $x/H=20$). DNS4000.

Chu (1989); Cafiero & Vassilicos (2019); Watanabe *et al.* (2014)) in figure 1. Note that entrainment conditions and Reynolds numbers are typically different between different experiments. The turbulent dissipation scaling has been computed on the centerline, and we have confirmed that C_ϵ is not constant but decreases along x while Re_δ increases. We have tried to fit different dissipation exponents m to the current simulation data; $m = 0.5$ was found to be the best exponent in a range between, approximately, $x/H = 19$ and $x/H = 32$ for DNS4000 (see figure 2). For DNS3000 there is no satisfactory power law fit over a reasonable x/H range for any value of m .

Turbulent / Non-turbulent interface and local interface velocity v_n

Different jet growth rates must be reflected in different entrainment and turbulent non-turbulent interface (TNTI, da Silva *et al.* (2014)) velocities. Following Zhou & Vassilicos (2017), we start from incompressibility $\partial u/\partial x + \partial v/\partial y + \partial w/\partial z = 0$ and obtain the following relation.

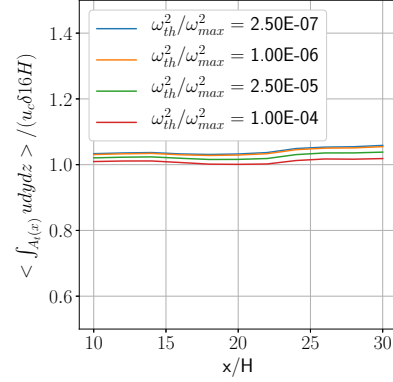


Figure 3. $\overline{\int_{A_t(x)} u dy dz} / (u_c \delta 16H)$ plotted along x/H for different enstrophy thresholds. DNS4000.

$$\frac{d}{dx} \overline{\int_{A_t(x)} u dy dz} = \mathcal{L} v_n \quad (4)$$

where $A_t(x)$ is the instantaneous area inside the TNTI, the overbar is an average over time, \mathcal{L} is the time-averaged interface length and v_n is a time and line-averaged local interface velocity. The self-similarity of the jet can be used to estimate the LHS of this equation (4): $\overline{\int_{A_t} u dy dz} \sim u_c A$ where $A \sim \delta H$ is the time averaged vortical area bounded by the TNTI, in good agreement with our DNS (see figure 3). Hence

$$\frac{d}{dx} (u_c \delta H) \sim \mathcal{L} v_n. \quad (5)$$

Given that we know δ and u_c from equations (2) and (3), we now need an estimate of the interface length \mathcal{L} in order to obtain the interface velocity v_n . We used our DNS to verify that the interface has a fractal structure and that $\mathcal{L} \sim H(\eta_l/\delta)^{1-D}$ where η_l is given by the Corrsin interface thickness estimate $\eta_l = v/v_n$, where v is the fluid's kinematic viscosity (Corrsin & Kistler (1955), see figure 4). Fractal dimensions of the interface were found between $D = 1.1$ and $D = 1.2$ (for different enstrophy threshold values characterizing the TNTI), D remaining constant along the streamwise direction. Substituting our fractal-Corrsin estimate of the interface length into equation (5), we obtain

$$\frac{v_n}{U_J} \sim Re_G^{(1-D)/D} ((x-x_0)/H)^{-\gamma_n} \quad (6)$$

where $\gamma_n = 2a + (1-3a)/D$. The local interface velocity depends on the global Reynolds number Re_G , fractal dimension D and the scaling exponent $a = a(m)$.

Taylor and Kolmogorov velocity scalings

Classical estimates of v_n assume it to be proportional to the Kolmogorov velocity $v_{\eta_{kol}} = (v\epsilon_0)^{1/4}$. Our equation (6) for the interface velocity agrees with the Kolmogorov

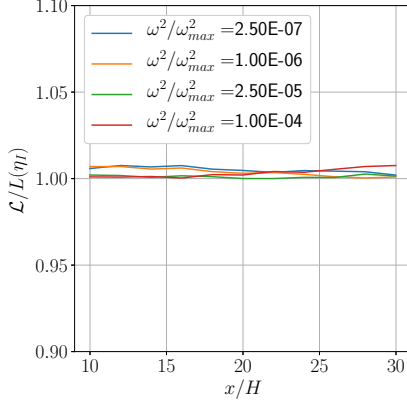


Figure 4. Comparison of actual interface length \mathcal{L} and Fractal-Corrsin estimate $L(\eta_I) = 16H(\eta_I/\delta)^{1-D}$ and $\eta_I = v/v_n$ for various enstrophy thresholds. DNS4000.

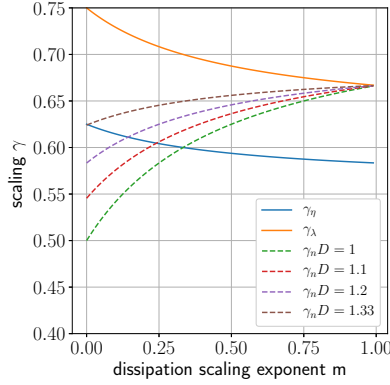


Figure 5. Velocity scaling exponent γ_n , see equation (6), plotted against the turbulence dissipation exponent m . Yellow solid line: scaling exponent for v_λ , blue solid line: scaling exponent for $v_{\eta_{kol}}$ and dashed lines: scaling exponent for v_n corresponding to different fractal dimensions $D=1.0, 1.1, 1.2, 1.33$ (bottom to top).

velocity estimate provided that $m = 0$ and $D = 4/3$. In the case of high Reynolds number non-equilibrium turbulence where $m = 1$, v_n is proportional to the Taylor velocity $v_\lambda = v/\lambda$ where $\varepsilon_0 \sim vK_0/\lambda^2$ irrespective of the value of D . The Reynolds number of our DNS is not high enough for $m = 1$. As already stated, we find $m = 0.5$. The TNTI velocity scaling therefore sits between the Kolmogorov and the Taylor velocity scalings and this is supported by our DNS (see figures 5 and 6).

TNTI and particle entrainment / detrainment

It is difficult to track fluctuations of the TNTI entrainment velocity around its mean value and we therefore track fluid elements which cross the interface and study their statistics. Enstrophy thresholds for the TNTI are determined by the area within a given normalised enstrophy threshold $\omega_{th}^2 \equiv \omega^2/\omega_{max}(x)^2$. The thresholds relevant to the TNTI are those for which this area does not vary much (see figure 8), ranging from the Laminar Superlayer (LSL, Corrsin & Kistler (1955)) to the Turbulent

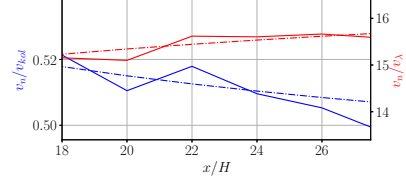


Figure 6. Ratio of velocities $v_n/v_{\eta_{kol}}$ and v_n/v_λ at threshold $\omega^2/\omega_{max}^2 = 2.5 \times 10^{-7}$. Blue and red dashed lines: theoretical scalings of $v_n/v_{\eta_{kol}}$ and v_n/v_λ . Blue and red solid lines: corresponding results from DNS4000.

Sublayer (TSL, Dairay *et al.* (2015)) region. These thresholds are normalised by $\overline{\omega_{max}(x)^2}$ which is the time-average maximum enstrophy in the $y-z$ plane at streamwise position x . Fluid elements are initially seeded outside in the potential flow region away from the interface region (see figure 7) and are tracked with Runge-Kutta 4 scheme. This is done in DNS3000 flow fields because the TNTI is defined by sharper enstrophy jumps in DNS3000 compared to DNS4000. Fluid element tracking was conducted for the duration of $120H/U_J$. The tracked fluid elements are grouped into four categories: N_{tt} is the number of fluid elements starting from a position where the flow is turbulent at time $t = 0$ and ending somewhere where the flow is also turbulent at time t ; N_{pp} is the number of fluid elements starting from a position where the flow is potential at time $t = 0$ and ending somewhere where the flow is also potential at time t ; similarly, N_{tp} corresponds to fluid elements going from turbulent to potential and N_{pt} from potential to turbulent. These four numbers are functions of time duration t and of normalised enstrophy $\omega^2/\omega_{max}(x)^2$ values at the start and at the end of tracking. The use of the words ‘‘potential’’ and ‘‘turbulent’’ in these definitions are only indicative and depend on threshold. For example, for a given enstrophy threshold ω_{th}^2 , fluid elements with normalised enstrophy values below this threshold at time $t = 0$ are considered to be in a potential state at that time while those with higher enstrophy values at that time are considered to be in a turbulent state. For this threshold and at that time there are N_t fluid elements in a turbulent state and N_p fluid elements in a potential state. The states of the fluid elements are evaluated in same way at time t .

$$\begin{aligned}
 N_{all} = & N_{tt}(t, \omega_{th}^2) \\
 & + N_{pp}(t, \omega_{th}^2) \\
 & + N_{tp}(t, \omega_{th}^2) \\
 & + N_{pt}(t, \omega_{th}^2)
 \end{aligned} \tag{7}$$

We find that N_{tp} and N_{pt} have a very marked peak just outside of the interface region, on the potential side (see figure 8). N_{tp} , which characterised detrainment, has a local minimum in the outer interface region but N_{pt} , which characterised entrainment, is about constant over more than one decade of the enstrophy thresholds at the outer side of the interface (see figure 8). Both have a peak at the inner interface region but this inner peak is by far much more pronounced in the detrainment than in the entrainment case. N_{tp} has no significant time dependence between the two peaks but N_{pt} does increase in time for all thresholds in

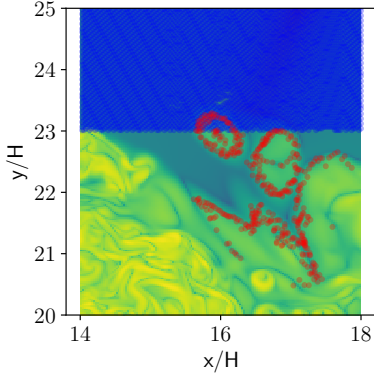


Figure 7. Seeding location compared to the instantaneous enstrophy field. Blue scatter points are initial location ($t = 0$) of the fluid elements. Red scatter points are locations in the band $1.14 \times 10^{-5} < \omega_{th}^2 < 2.78 \times 10^{-5}$ at time $t = 12H/U_J$. DNS3000.

agreement with the fact that entrainment dominates overall. However, the peak of N_{tp} at the inner interface region also increases very significantly with time, indicating that local detrainment events increase with time on the turbulent side of the interface. The ratio of entrainment to detrainment at the peak of detrainment, i.e. N_{tp}/N_{pt} where N_{tp} is maximum on the inner side of the interface, is around 3, which suggests that detrainment is significant in the inner interface region. This means that fluid elements are captured in the inner side of the interface for a relatively long time before being eventually entrained.

Column Breaking Method

In order to study the entrainment and detrainment characteristics of the interface more locally, we introduce the column breaking method. A column of fluid elements is defined by the set of the fluid elements between two iso-enstrophy surfaces, both enstrophy thresholds defining these two iso-surfaces being within the TNTI range of enstrophy thresholds. The normalised enstrophy at every fluid element inside this column lies, therefore, between these two normalised enstrophy thresholds. Defining this column at time t_0 and letting time evolve, this column breaks down into persisting (or remaining), entrained and detrained fluid elements. The persisting/remaining fluid elements are those where the normalised enstrophy remains within the original column's range of normalised enstrophies. The entrained fluid elements are those where the normalised enstrophy is higher and the detrained fluid elements are those where the normalised enstrophy is lower than the range of normalised enstrophies inside the original column (see figure 9). Ensemble statistics were taken by considering different time origins $t_0 = 12i \times H/U_J$ ($i = 1, 2, \dots, 9$) for the duration of $12H/U_J$. Defining the number $N(t_0)$ of fluid elements in the column at the initial time t_0 ,

$$P + E + D = \frac{N_P(t_1 - t_0)}{N_P(t_0)} + \frac{N_E(t_1 - t_0)}{N_P(t_0)} + \frac{N_D(t_1 - t_0)}{N_P(t_0)} = 1 \quad (8)$$

where P , E and D are, respectively, the fractions of persisting, entrained and detrained fluid elements at time $t_1 > t_0$. Figure 10 shows the time evolution of the average val-

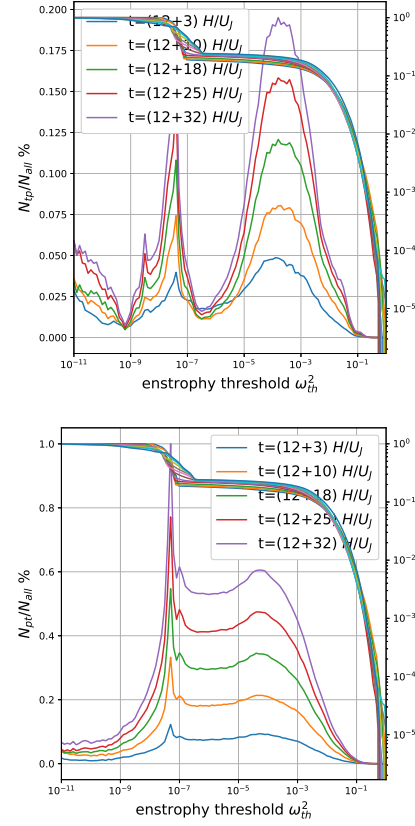


Figure 8. Left axis: N_{tp}/N_{all} (top, detrainment) and N_{pt}/N_{all} (bottom, entrainment) versus normalised enstrophy threshold ω_{th}^2 . Different colours correspond to different times. Right axis: Area of the region in the y - z plane where the enstrophy is above the enstrophy threshold, at different x/H locations. DNS3000.

ues (over the ensemble statistics mentioned two sentences above) of P , E and D for two normalised enstrophy threshold bands, $\omega_{th}^2 = 3.16 \times 10^{-7}$ to $\omega_{th}^2 = 7.74 \times 10^{-7}$ characterising the outer (towards potential) side of the TNTI and 4.08×10^{-4} to 10^{-3} characterising the inner (towards turbulent) side of the TNTI. As we can expect from the results in the previous section, detrainment is much weaker than entrainment at the outer side of the interface but comparable to entrainment at the inner side of the interface as time advances (see figure 10). This tendency is also evident in figure 11 where the average P , E and D are plotted at two times as functions of normalised threshold. Entrainment is decreasing whereas detrainment is increasing with increasing threshold, i.e. as one moves from the outer to the inner sides of the TNTI. In fact, entrainment and detrainment tend to equalise at the inner side of the interface. It is also significant that the persistence increases towards the inner side of the interface, which suggests that fluid elements are somehow trapped and spend longer times there.

Threshold crossings

To study column breaking in a little more detail, we present histograms of numbers of consecutive fluid element crossings through the higher and lower enstrophy sides of the threshold band defining the initial column, see figure 12. On the lower enstrophy side of the band, even numbers

of consecutive crossings (fluid elements which are detrained and entrained again) occur more frequently than odd numbers (fluid elements which are detrained). This tendency is much stronger at low threshold values, i.e. near the outer, potential side, of the TNTI, than at high threshold values near the inner, turbulent side, of the TNTI. However, the chance of an odd number of crossings leading to a detrainment event is neither zero nor negligible. On the other hand, on the higher enstrophy side of the band, odd numbers of consecutive crossings (fluid elements which are entrained) occur more frequently than even numbers (fluid elements which keep crossing and resist entrainment). Again, this tendency is much stronger at the lower rather than at the higher enstrophy levels of the TNTI. However the chance of fluid elements crossing the higher side of the enstrophy band an even number of times and thereby resisting entrainment for a while is not negligible.

Finally, note that there are more consecutive crossings in the inner, turbulent, side of the TNTI than in its outer, potential, side. The entrainment process is much more complex on the turbulent side of the TNTI where it is much less smooth and direct than on the TNTI's potential side. Furthermore, even if rare, there are fluid element trajectories which cross a large number of times on both sides.

Band crossings

We now investigate the number of fluid elements which consecutively cross both sides of the band. For this analysis, we fix the higher enstrophy threshold of the band to $\omega_{th}^2 = 1.00 \times 10^{-3}$ and vary the lower enstrophy threshold. The counting method is different from the one used for threshold crossings in the previous section, see figure 13 for an indication. As one might expect, the number of fluid elements which cross both higher and lower threshold sides is less when the band is wider (see figure 14). This number, even if relatively small, is definitely finite. The number of such crossings can increase up to six when the lower enstrophy threshold of the present band increases to 4.08×10^{-4} . In fact, the total number of these crossings increases quite fast with lower enstrophy threshold (see figure 15).

Conclusion

We have established and validated a way to estimate the average local interface velocity v_n in turbulent planar jets theoretically and numerically. The scalings of this entrainment velocity are closely related to the equilibrium or non-equilibrium nature of the turbulent dissipation.

The dynamics of the TNTI are indirectly investigated by fluid element tracking. We found smooth and dominant entrainment in the outer, potential, side of the TNTI where the interface is itself relatively smooth, and complex entrainment and detrainment dynamics in the inner, turbulent, side of the TNTI where the interface is itself quite rough. Entrainment and detrainment tend to balance in the inner side of the interface, indicating some potential fluid element trapping mechanism at the TNTI which is consistent with the fact that the mean lateral velocity is zero on the sides of the jet and that inner iso-enstrophy contours have relatively high fractal dimensions whereas the fractal dimension of the outer iso-enstrophy contours is low.

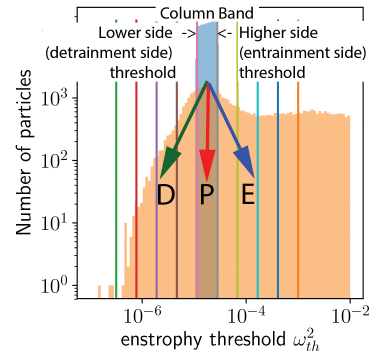


Figure 9. Example of column breaking analysis. The blue histograms shows a column in the band of thresholds $1.14 \times 10^{-5} < \omega_{th}^2 < 2.78 \times 10^{-5}$ at time $t = 12H/U_J$. The orange histograms shows its breaking down at time $t = 24H/U_J$. DNS3000.

REFERENCES

- Cafiero, G. & Vassilicos, J. C. 2019 Non-equilibrium turbulence scalings and self-similarity in turbulent planar jets. *Proceedings of the royal society A* **475**.
- Corsin, S. & Kistler, A. L. 1955 Free-Stream Boundaries of Turbulent Flows. *NACA-report-1244*.
- Dairay, T., Obligado, M. & Vassilicos, J. C. 2015 Non-equilibrium scaling laws in axisymmetric turbulent wakes. *Journal of Fluid Mechanics* **781**, 166–195.
- George, W. K. 1989 The self-preservation of turbulent flows and its relation to initial conditions and coherent structures. *Advances in turbulence* **3973**.
- Klein, M., Sadiki, A. & Janicka, J. 2003 A digital filter based generation of inflow data for spatially developing direct numerical or large eddy simulations. *Journal of computational Physics* **186** (2), 652–665.
- da Silva, Carlos B., Hunt, Julian C.R., Eames, Ian & Westerweel, Jerry 2014 Interfacial Layers Between Regions of Different Turbulence Intensity. *Annual Review of Fluid Mechanics* **46** (1), 567–590.
- Thomas, FO & Chu, HC 1989 An experimental investigation of the transition of a planar jet: Subharmonic suppression and upstream feedback. *Physics of Fluids A: Fluid Dynamics* **1** (9), 1566–1587.
- Townsend, A.A. 1976 The structure of turbulent shear flow, 2nd edition. by a. a. townsend. cambridge university press, 1976. 429. *Journal of Fluid Mechanics* **76** (3), 622624.
- Vassilicos, J. C. 2015 Dissipation in turbulent flows. *Annual Review of Fluid Mechanics* **47**, 95–114.
- Watanabe, Tomoaki, Sakai, Yasuhiko, Nagata, Kouji, Ito, Yasumasa & Hayase, Toshiyuki 2014 Vortex stretching and compression near the turbulent/non-turbulent interface in a planar jet. *Journal of Fluid Mechanics* **758**, 754–785.
- Zhou, Y. & Vassilicos, J. C. 2017 Related self-similar statistics of the turbulent/non-turbulent interface and the turbulence dissipation. *Journal of Fluid Mechanics* **821** (2011), 440–457.

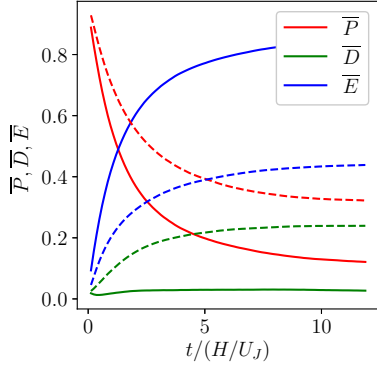


Figure 10. Average values of persistence P (red), entrainment E (green) and detrainment D (blue) at threshold bands $\omega_{th}^2 = 3.16 \times 10^{-7}$ to $\omega_{th}^2 = 7.74 \times 10^{-7}$ (solid lines) and 4.08×10^{-4} to 10^{-3} (dashed lines). DNS3000.

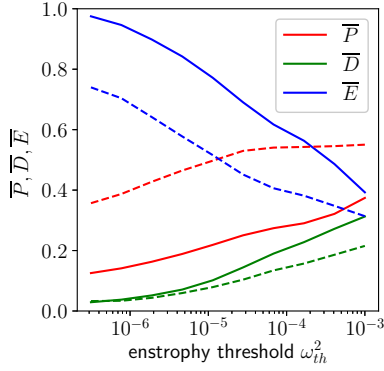


Figure 11. Average values of persistence P (red), entrainment E (green) and detrainment D (blue) for threshold bands ω_{th}^2 to $2.448\omega_{th}^2$ at times $t = 2.4H/U_J$ (dashed line) and $12H/U_J$ (solid line) plotted against outer side entrophy threshold ω_{th}^2 . DNS3000.

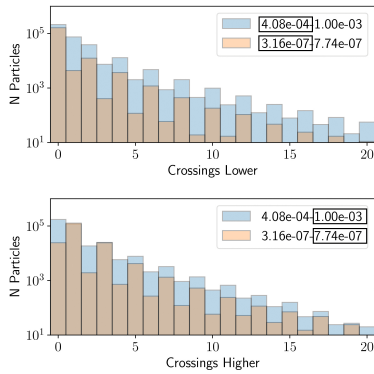


Figure 12. Histograms of number of consecutive fluid element crossings through the lower entrophy side (top) and higher entrophy side (bottom) of the threshold band for two different threshold bands: one toward the outer, potential, side of the TNTI ($\omega_{th}^2 = 3.16 \times 10^{-7}$ to 7.74×10^{-7}) and one towards the inner, turbulent, side of the TNTI ($\omega_{th}^2 = 4.08 \times 10^{-4}$ to 10^{-3}). The total number of fluid element samples is $N_{all} = 3.6 \times 10^5$ and 1.9×10^5 respectively. DNS3000.

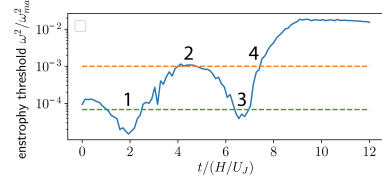


Figure 13. Sample fluid element which crosses the band's borders consecutively from lower threshold border to higher threshold border four times. DNS3000.

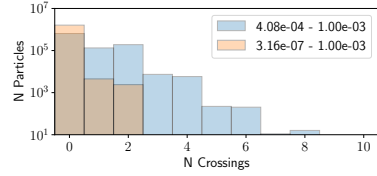


Figure 14. Histograms of band crossings for the bands $4.08 \times 10^{-4} < \omega_{th}^2 < 1.00 \times 10^{-3}$ (blue) and $4.08 \times 10^{-4} < \omega_{th}^2 < 1.00 \times 10^{-3}$ (red). The total number of samples is $N_{all} = 1.6 \times 10^6$. DNS3000.

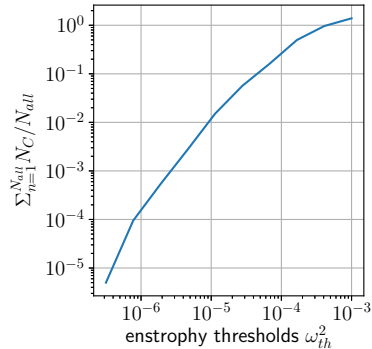


Figure 15. Sum of crossings in figure 14 plotted against the lower entrophy threshold of the band. The higher entrophy threshold is fixed to $\omega_{th}^2 = 1.00 \times 10^{-3}$. DNS3000.